Progress in Reaction Kinetics and Mechanism

ARTICLE

Open Access

https://doi.org/10.48130/prkm-0026-0007

Progress in Reaction Kinetics and Mechanism **2026**, 51: e013

Performance and mechanism of constructing an adsorption site with Ca-modified $LaMnO_3$ to efficiently adsorb phytic acid: Ca doping and loading for acidic and alkaline water bodies, respectively

Menghan Feng[1,2#], Shiyu Lv[1,2,3#], Xueyan Zhang[1,2], Changbin Guo[1,2,4], Tian Yuan[1,2,5], Weilin Fu[1], Jien Zhou[1,4], Yanli Luo[4] and Feng Wang[1,2*]

[1] *Agro-Environmental Protection Institute, Ministry of Agriculture and Rural Affairs, Tianjin 300191, China*
[2] *Agro-Ecosystem, National Observation and Research Station, Dali 671004, China*
[3] *College of Resources and Environment, Yunnan Agricultural University, Kunming 650201, China*
[4] *College of Resources and Environment, Xinjiang Agricultural University, Urumqi 830052, China*
[5] *College of Resources and Environment, Shanxi Agricultural University, Jinzhong 030801, China*
[#] Authors contributed equally: Menghan Feng, Shiyu Lv
[*] Correspondence: wangfeng_530@163.com (Wang F)

Abstract

Ca-doped and Ca-loaded $LaMnO_3$ (CLMO and CaO-LMO) were derived from $LaMnO_3$ (LMO) and synthesized by coprecipitation and doping. Batch adsorption tests revealed that CLMO exhibited superior adsorption capabilities for phytic acid in acidic water, with an adsorption capacity of 86.54 mg P/g at pH 3, representing 63% and 130% increases over those of LMO and CaO-LMO, respectively. Conversely, CaO-LMO demonstrated an enhanced adsorption performance in neutral to alkaline water with an adsorption capacity of 83.20 mg P/g at pH 10, which was 810% and 111% higher than those of LMO and CLMO, respectively. The adsorption of phytic acid by all three perovskites was characterized as monolayer chemical adsorption, involving mechanisms such as ligand exchange, inner sphere complexation, and electrostatic attraction. X-ray diffractometry, X-ray photoemission spectroscopy, and Fourier transform infrared spectroscopy confirmed that the primary adsorption sites for phytic acid were the La/Ca sites and oxygen vacancies in CLMO, the La/Ca sites in CaO-LMO, and the La sites in LMO. Ca doping/loading enriched the active sites for phytic acid adsorption and enhanced the structural stability of the materials. CLMO and CaO-LMO exhibited excellent performance in recovering different forms of organic phosphorus from various real wastewater sources under dynamic adsorption conditions. The results suggest that CLMO should be prioritized for organic phosphorus removal in acidic waters, whereas CaO-LMO should be prioritized for the same in alkaline waters. This research provides a technical solution for the efficient recovery of organic phosphorus from water bodies.

Citation: Feng M, Lv S, Zhang X, Guo C, Yuan T, et al. 2026. Performance and mechanism of constructing an adsorption site with Ca-modified $LaMnO_3$ to efficiently adsorb phytic acid: Ca doping and loading for acidic and alkaline water bodies, respectively. *Progress in Reaction Kinetics and Mechanism* 51: e013 https://doi.org/10.48130/prkm-0026-0007

Introduction

Phosphorus (P) in aquatic ecosystems acts as an energy transmitter in biological growth processes. P is categorized as either inorganic or organic, with the latter exhibiting high water solubility, degradation resistance, and persistent toxicity, allowing it to persist in the environment for extended periods. Phytic acid is the most abundant form of organic phosphorus in the soil and constitutes > 50% of the organic phosphorus pool in the soil. Phytic acid—also known as myo-inositol hexakisphosphate ($C_6H_{18}O_{24}P_6$)—is a phosphoric monoester frequently found in soil resulting from the deposition of plant-derived materials[1,2]. Excessive phytic acid runoff and erosion losses transport phosphorus into water bodies, leading to water eutrophication and phosphorus pollution, which threaten clean agricultural production as well as human life and health[3]. Agencies such as the United States Environmental Protection Agency have established thresholds for total phosphorus levels in lakes and natural water bodies[4]. Since it is a nonrenewable resource, the excessive exploitation of phosphorus has resulted in a decrease in its reserves[5]. Some studies have explored the immobilization of phosphate in the soil; however, minimal attention has been paid to organic phosphorus loss in water bodies and its prevention and control[6,7]. Functional materials must be developed for the recovery of phytic acid from wastewater to reduce phosphorus pollution, maintain environmental ecological stability, and sustainably use phosphorus resources.

Adsorbents such as fly ash, gypsum[8], dolomite[9], and zeolite[10] have been utilized to immobilize phytic acid in the soil, primarily relying on the interaction of the metal ions in metal oxides or hydroxides with phosphate groups. Using a calcite–water interface for phytic acid adsorption suffers from remarkable drawbacks, such as narrow pH applicability, low capacity, or unclear active sites[11,12]. The applicability of these materials in aquatic environments remains uncertain. Additive modification is the most suitable method to overcome these deficiencies and typically involves doping[13] and loading[14]. Additives can either be doped into the lattice or loaded onto the surface to form separate phases. Loading, doping, or their induced defects can regulate the electronic structure of a material to some extent to enhance phosphorus adsorption[15]. The preparation of $LaCeO_x$ heterostructured hierarchical carbon composites (L_8C_2PC) through loading resulted in a 54% increase in phosphate adsorption capacity, which was attributed to the increased electron density at the La sites that enriched the active centers[16]. Doping Fe into the CoO lattice and loading Co hydroxide on iron oxide enhanced the hydrogen evolution reaction, thus expanding the applicable pH range and clarifying the reaction sites[17]. Different

modification methods may lead to different adsorption active sites in the same base material, thereby resulting in different adsorption behaviors of adsorbents for phosphates. However, there is currently a lack of research on the active sites for adsorption resulting from different modification methods.

As a class of metal oxides, ABO_3-type perovskites exhibit superior structural stability compared with single-metal oxides and offer greater potential for modulation of the electronic structure[18]. Lanthanide elements (La, Pr, and Gd) and alkaline earth metals (Ca, Sr, and Ba) are frequently chosen for the A-site of perovskites. Meanwhile, the B-site typically consists of transition metals (Ti, Mn, and Ir). La, a rare earth metal, possesses a high surface charge density, stable oxidation states, and Lewis acidity, making it adept at accepting paired electrons[19]. In addition, it has a high affinity for phosphates and is increasingly recognized for its role in phosphate adsorption. Our previous research involved the synthesis of $LaFeO_3$ and $LaMnO_3$ via sol–gel and hydrothermal methods, respectively, and the enhancement of their phosphate adsorption properties through doping with elements such as Al and Ni[15,20]. Organic phosphates such as phytic acid are prevalent in agricultural production and wastewater treatment but have been under-researched. Their many phosphate functional groups and high reactivity present challenges to understanding their binding characteristics and mechanisms and the applicability of reaction conditions with materials. Ca, because of its low cost and minimal environmental impact, is considered to be a promising element for material modification. Studies have shown that Ca modification can effectively enhance the physical and chemical properties of materials, increase the specific surface area[15], optimize pore structure[19], and enhance the stability of perovskite structures[20], thereby significantly improving their phosphate adsorption capacity. However, further research is needed on the performance and mechanism of Ca-modified $LaMnO_3$ in phytate adsorption. This study prepared $LaMnO_3$ through Ca doping and loading modifications, compared the physicochemical properties of different materials, and analyzed the kinetics, thermodynamics, and influencing factors of phytic acid adsorption via batch adsorption experiments. The findings elucidate the changes in electronic structure induced by doping and loading and confirm the mechanism of phytic acid adsorption through the construction of active sites.

Materials and methods

Preparation of experimental reagents and materials

The primary reagents used in the experiments were $La(NO_3)_3{\cdot}6H_2O$, $CaCl_2$, CaO, $Mn(NO_3)_2{\cdot}4H_2O$, absolute ethanol, ethylene glycol, citric acid, and urea. Detailed information on the reagents and preparation methods can be found in Supplementary Material S1.

Batch adsorption experiments

In brief, 0.02 g of $LaMnO_3$ (LMO), Ca-doped $LaMnO_3$ (CLMO), and Ca-loaded $LaMnO_3$ (CaO-LMO) were separately weighed into 50-mL conical flasks and added to 50 mL of phytic acid solution at a concentration of 5–300 mg/L with pH values of 3, 7, and 10, respectively. Samples were taken at intervals of 0–2,880 min. Next, the flasks were placed in a shaking incubator at 25 °C and 180 rpm. The supernatant was filtered through a 0.45-μm membrane filter, and the concentration of phosphorus was determined by ammonium molybdate spectrophotometry. The experiment was repeated three times. The experimental data were fitted using the Langmuir (2-1), Freundlich (2-2), and Dubinin–Radushkevich (D-R; 2-3) isothermal adsorption equations and pseudo-first-order (2-6), pseudo-second-order (2-7), and intraparticle diffusion (2-8) kinetic models[21,22]. Further details on the adsorption fitting experiments are provided in Supplementary Material S2.

Field water testing

Samples of pond runoff wastewater, domestic sewage effluent, and cattle farm wastewater were collected from a test station in Dali City, Yunnan Province, China. Their pH values were 8.03 ± 0.02, 8.01 ± 0.03, and 8.05 ± 0.02 and the total phosphorus concentrations were 0.444 ± 0.025, 6.012 ± 0.271, and 19.84 ± 0.162 mg P/L, respectively. In a conical flask, adsorbents at the following doses were added to the water samples: 0.01, 0.05, 0.1, 0.2, and 0.4 g/L added to 100 mL of pond runoff wastewater; 0.1, 0.2, 0.4, 1, and 2 g/L to 100 mL of domestic sewage effluent; and 0.4, 1, 2, 4, and 6 g/L to 100 mL of cattle farm wastewater. The mixtures were cultured in a constant-temperature incubator (25 ± 0.5 °C) at 180 rpm for 24 h. The remaining total phosphorus concentrations were measured, and the total phosphorus removal rates were calculated. The experiment was conducted under the same conditions as described above and repeated three times.

Fixed-bed column tests

In brief, 0.5 g of CLMO was loaded onto a polyethylene column with a length of 10 cm and an inner diameter of 10 mm. A peristaltic pump was adjusted to pump the phytic acid solution (pH = 3, C_0 = 100 mg/L) upward at a flow rate of 2 mL/min. Samples were collected at regular intervals from the outlet of the column, starting from the point where the liquid began to flow out. The remaining phytic acid concentrations were determined. The experiment was conducted under the same conditions as destribed above and repeated three times.

Multiple organic phosphorus removal tests

In brief, 0.02 g of each adsorbents was placed in conical flasks, to which 50 mL of various solutions containing glucose-6-phosphate (G_6P), adenosine triphosphate (ATP), and etidronic acid (HEDP) were added at an initial concentration of 100 mg/L. The pH of the solutions was adjusted to 7 to investigate the adsorption performance of the adsorbents for different organic phosphates. The experiment was conducted under the same conditions as described above and repeated three times.

Characterization of adsorbents

The characteristics of the three adsorbents before and after phytic acid adsorption were investigated via various characterization techniques to elucidate their adsorption mechanisms. Instrumentation and details of the characterization methods are provided in Supplementary Material S3.

Results and discussion

Physicochemical properties of Ca-doped/loaded $LaMnO_3$

Figure 1a–c presents the morphology and microstructure of the three adsorbents observed using scanning electron microscopy

(SEM). The surface of the $LaMnO_3$ exhibited a porous structure with unevenly distributed and variably sized pores, which was observed in the scanning thickness range of electron microscopy (Fig. 1a). Upon Ca doping, the CLMO's surface showed micron-sized pores deposited with porous granular material (Fig. 1b). After CaO loading, the pores were filled with uniformly dense blocky material (Fig. 1c). The X-ray diffraction (XRD) analysis (Fig. 1d) indicated that all three adsorbents had clear phases and high crystallinity, with diffraction peaks centered at 22.9°, 32.6°, 40.2°, 46.8°, 58.2°, and 68.3°, corresponding to the monoclinic space group $P2_1/a$ of $LaMnO_3$ (JCPDS No. 97-015-0260)[23]. CaO-LMO exhibited characteristic peaks at 29.3° and 48.8°, corresponding to the hexagonal space group $R\bar{3}c$ of $CaCO_3$ (JCPDS No. 97-004-0543)[24], suggesting that Ca was loaded onto $LaMnO_3$ as $CaCO_3$. No characteristic diffraction peak of $CaCO_3$ was detected at 29.3° for CLMO, indicating that Ca had replaced the $LaMnO_3$ lattice. The characteristic peaks of CLMO shifted to the right relative to those of LMO, suggesting that Ca^{2+} (99Å) with a small ionic radius had replaced some La^{3+} (106Å) with a large ionic radius[25]—a phenomenon also confirmed by Londoño-Calderón et al. All three adsorbents exhibited Type IV adsorption–desorption isotherms (Fig. 1e) with a significant H3 hysteresis loop, indicating the presence of a porous structure[26]. The isotherms indicate weak N_2 adsorption at low relative pressures, which indicates monolayer adsorption behavior. A pronounced hysteresis loop was observed within a significantly elevated relative pressure range and was attributed to the gradual appearance of secondary disordered mesoporous layers. The pore size distribution curves revealed that LMO and CLMO had dense micropores and mesopores, and CaO-LMO contained a large number of micropores, mesopores, and macropores. The specific surface area, pore size, and pore volume of CLMO were significantly higher than those of LMO (Supplementary Table S1), and the N_2 adsorption capacity of CaO-LMO was notably reduced because of the blockage of pore channels by $CaCO_3$. Fourier transform infrared (FTIR) spectroscopy provided information on the bonding between metal and oxygen ions in the structural lattice (Fig. 1f). The infrared absorption bands at 400–650 cm^{-1} within the $LaMnO_3$ structure were attributed to the MnO_6 octahedral units present in the perovskite lattice[27]. Compared with those

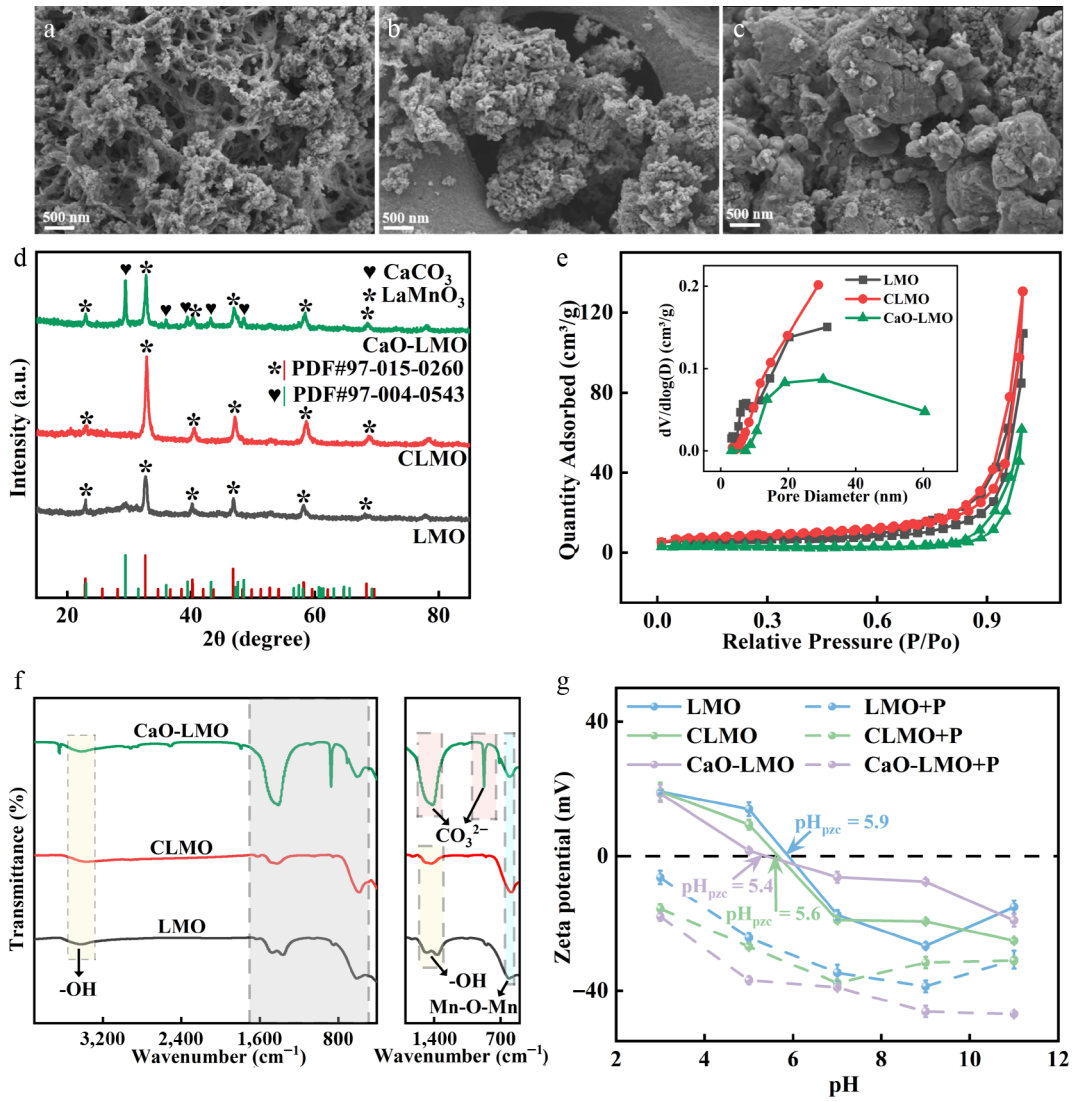

Fig. 1 Scanning electron microscopy patterns of (a) LMO, (b) CLMO, and (c) CaO-LMO. (d) XRD patterns of materials in the 2θ range from 15° to 85°. (e) N_2 adsorption–desorption isotherm. (f) FTIR images covering the full range from 410 to 3,900 cm^{-1}; the magnified view on the right-hand side ranges from 500 to 1,700 cm^{-1}. (g) Zeta potential, for which the measurement points were set at pH 3, 5, 7, 9, and 11 (the solid line is the zeta potential before adsorption of phytic acid, and the dashed line is the zeta potential after adsorption of phytic acid).

in LMO, the Mn–O bands in CLMO exhibited a slight rightward shift, resulting from the disrupted symmetry of the $LaMnO_3$ lattice caused by Ca doping, leading to differences in coordination number, metal–oxygen (M–O) bond lengths, and crystal distortion[28]. Shi et al. confirmed that Mn doping into the crystal structure of $LaFeO_3$ changes the lengths of Fe–O and La–O[29]. The characteristic peaks of CaO-LMO at 850–900 and 1,350–1,550 cm^{-1} correspond to typical CO_3^{2-} signals, which are associated with $\nu_2(CO_3)$ and $\nu_3(CO_3)$ vibrations[30]. This finding further confirmed that Ca was loaded onto $LaMnO_3$ as $CaCO_3$, corroborating the XRD results. The spectral broadbands of the three adsorbents at 3,700–2,800 and 1,640 cm^{-1} were attributed to the O–H stretching of water and the bending vibration of H–O–H, respectively[17].According to the zeta potential data in the far-right column of Fig. 1g, the isoelectric points of LMO, CLMO, and CaO-LMO are 5.9, 5.6, and 5.4, respectively, indicating that these materials exhibit similar surface charge properties. When the pH of the solution is lower than the isoelectric point (pHpzc), the material surface typically carries a positive charge, resulting in weaker repulsive forces between colloidal particles. Conversely, when the pH exceeds pHpzc, the surface of the colloidal particles typically carries a negative charge, indicating enhanced repulsive forces between particles.

X-ray photoemission spectroscopy (XPS analysis) was conducted to evaluate the elemental composition and chemical states of the surfaces of the three adsorbents, as shown in Fig. 2a–d. Detailed fitting information can be found in Supplementary Material S4. The XPS results were then calibrated using the C 1s binding energy value (284.8 eV). The Ca 2p spectrum of CLMO had peaks at 349.6 and 346.3 eV (Fig. 2a), which correspond to the binding energies of Ca 2p1/2 and Ca 2p3/2, with a spin-orbit splitting value of approximately 3.3 eV. Similarly, CaO-LMO showed peaks at 350.1 and 347.0 eV, representing Ca 2p1/2 and Ca 2p3/2 with a spin-orbit splitting of approximately 3.1 eV. These results indicated that most Ca ions in CLMO and CaO-LMO were in the +2 spin-orbit[31]. However, the XPS spectral positions of Ca in these two materials differed significantly, with CaO-LMO exhibiting a shift toward higher binding energies than CLMO. This finding suggests that different forms of Ca combine with $LaMnO_3$. The binding energy peaks of Ca in CLMO (346.3 and 349.6 eV) are similar to those reported by Bai et al. for Ca^{2+}-doped $LaCrO_3$ (346.6 and 350.2 eV), indicating that Ca was incorporated into the $LaMnO_3$ lattice as a dopant[32]. CLMO and CaO-LMO showed a shift of La toward lower binding energies compared with LMO (Fig. 2b, c), indicating that Ca doping and loading affect the La structure. In CLMO, Mn shifted toward higher binding energies, suggesting that the substitution of Ca^{2+} for some La^{3+} leads to charge imbalance, which is compensated by the oxidation of multivalent Mn or the formation of oxygen vacancies, resulting in a shift in the Mn binding energy[33]. However, no shift in the Mn binding energy was observed in CaO-LMO. The fine O 1s spectra of all three adsorbents exhibited two peaks (Fig. 2d) corresponding to the two chemical states of oxygen. The low and high peaks (529.0–529.3 and 531.0–531.4 eV) were attributed to surface lattice oxygen (O_{latt}) and adsorbed oxygen (O_{ads}) in the surface oxygen vacancies[34]. In the spectrum, no typical peaks for Ca–O and La–O lattice oxygen were detected, possibly because of the formation of a La–O–Ca interface structure, where Ca and La share an oxygen atom. We observed that the peak positions of CaO-LMO and LMO were similar, with no significant changes. By contrast, the O_{latt} peak of CLMO significantly shifted toward higher binding energies, indicating that doping alters the O structure in CLMO. This finding is consistent with the study by Wang et al.[35]. Therefore, loading does not significantly affect the material's structure, and doping significantly modifies the structural forms of La and O in $LaMnO_3$.

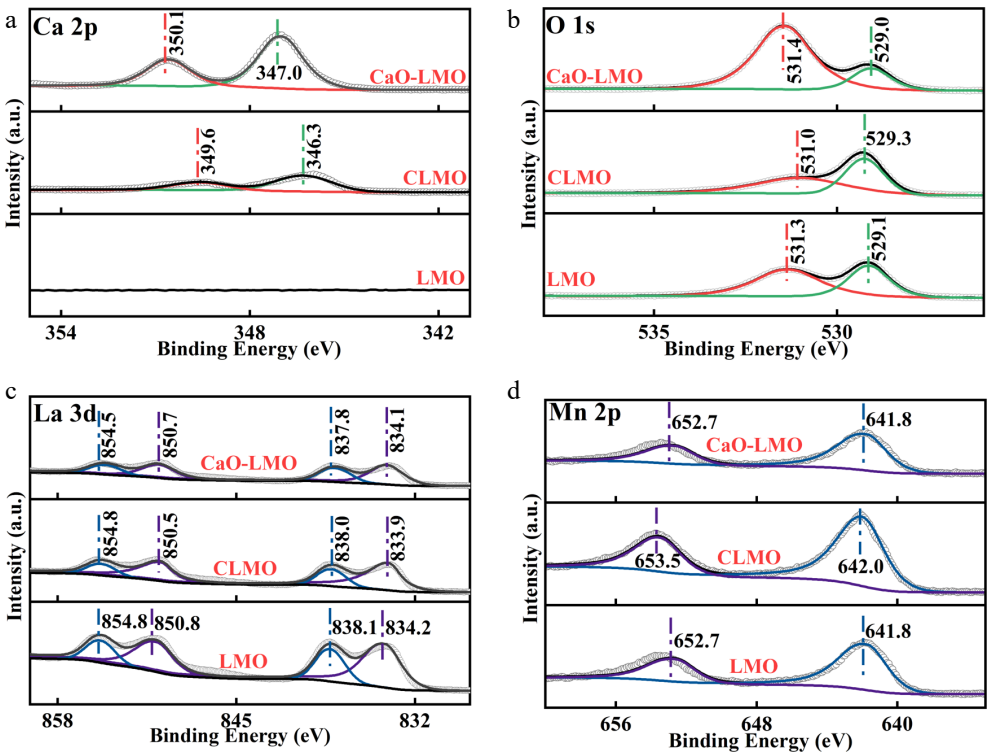

Fig. 2 XPS results for (a) Ca 2p, (b) La 3d, (c) Mn 2p, and (d) O 1s of the materials. All peaks were corrected by the C 1s peak (284.8 eV) and subjected to deconvolution.

Characterization of adsorbents

Adsorption isotherms are crucial for understanding adsorption characteristics. By comparing and analyzing the fitting effects and applicability of the Langmuir, Freundlich, and Dubinin–Radushkevich models in simulating phosphate adsorption, the intrinsic nature and mechanisms of the adsorption process can be thoroughly elucidated. This study measured the isotherms for phytic acid adsorption on materials at three pH levels (Fig. 3a, b), with the data fitted using the nonlinear models of Langmuir, Freundlich, and Dubinin–Radushkevich (Supplementary Table S2). At pH values of 3, 7, and 10, the Langmuir and Dubinin–Radushkevich models adequately describe the adsorption of phytic acid on LMO, CLMO, and CaO-LMO, indicating that the adsorption is primarily monolayer chemisorption. The values of E (kJ/mol) provided insights into the adsorption mechanism. The average adsorption energies for LMO, CLMO, and CaO-LMO had $E > 18$ kJ/mol, suggesting that the adsorption was mediated by a chemical reaction. The pH significantly influenced the adsorption performance of the three adsorbents. At pH 3, the adsorption capacity of LMO for phytic acid was 53.05 mg P/g, which decreased significantly as the pH increased to 7 and 10. Compared with those of LMO, the adsorption capacities of CLMO increased by 63%, 153%, and 330% at pH 3, 7, and 10, respectively, indicating that doping enhances the capacity for phytic acid adsorption across a wide pH range, overcoming the weakness of the original $LaMnO_3$ in alkaline conditions. CaO-LMO exhibited a substantial enhancement in the capacity for phytic acid adsorption at pH 7 and 10, with increases of 320% and 810% relative to those of the original $LaMnO_3$, indicating improved adsorption capacity under moderately alkaline conditions.

To gain a deeper understanding of the phosphate adsorption behavior of adsorbent surfaces, selecting an appropriate adsorption kinetics model is crucial for optimizing the adsorption conditions and enhancing the adsorption efficiency. According to the fitting results of the pseudo-first-order, pseudo-second-order, and Weber–Morris kinetic adsorption models (Fig. 4), the regression coefficient R^2 of the pseudo-second-order model was higher than that of the pseudo-first-order model (Supplementary Table S3). In addition, the Q_e of the pseudo-second-order model is closer to the actual adsorption capacity, indicating that the adsorption of phytic acid by the three adsorbents was consistent with chemical adsorption, where the ions and adsorbent functional groups share or exchange electrons as covalent forces, similar to phosphate adsorption (Fig. 4a). Considering that the Weber–Morris model is only applicable to the initial stage of adsorption reactions, this study only analyzed the fitting results for the first two stages[36]. As shown in Supplementary Table S3, at pH 3 and 7, all three materials exhibited the characteristics of intraparticle diffusion during the initial stage. However, at pH 10, the fitting results for CaO-LMO were poor, indicating that the initial adsorption of phytic acid by CaO-LMO at pH 10 was primarily controlled by chemisorption rather than intraparticle diffusion. During the adsorption of phytic acid by the three adsorbents (Fig. 4b), the concentration gradient was large during the initial stage; therefore, the slope of the first stage (the movement of ions from the solution to the material surface) was the largest. The second stage corresponded to intraparticle diffusion, where the adsorption rate significantly slowed down ($K_{i,2} < K_{i,1}$), suggesting that this process primarily controls the adsorption rate. When the adsorption rate decreases to a certain value, the adsorption rate equals the desorption rate, and the adsorption reaches equilibrium. Furthermore, the fitting results showed that the intercepts of all parts were not zero (Supplementary Table S3), indicating that intraparticle diffusion is one of the rate-controlling steps in adsorption.

Considering the complexity of real aquatic environments, factors such as pH and coexisting ions can influence materials' efficiency in phytic acid adsorption. To address this, we systematically introduced these factors under laboratory conditions to investigate the adsorption and selectivity of materials under different influences. Additionally, we conducted experiments on the adsorption of various types of organophosphorus compounds by tests with the material and actual wastewater treatment to verify its broad applicability in complex aquatic environments.

The influence of the solutions' initial pH on the adsorption of phytic acid by LMO, CLMO, and CaO-LMO is depicted in Fig. 5c. The

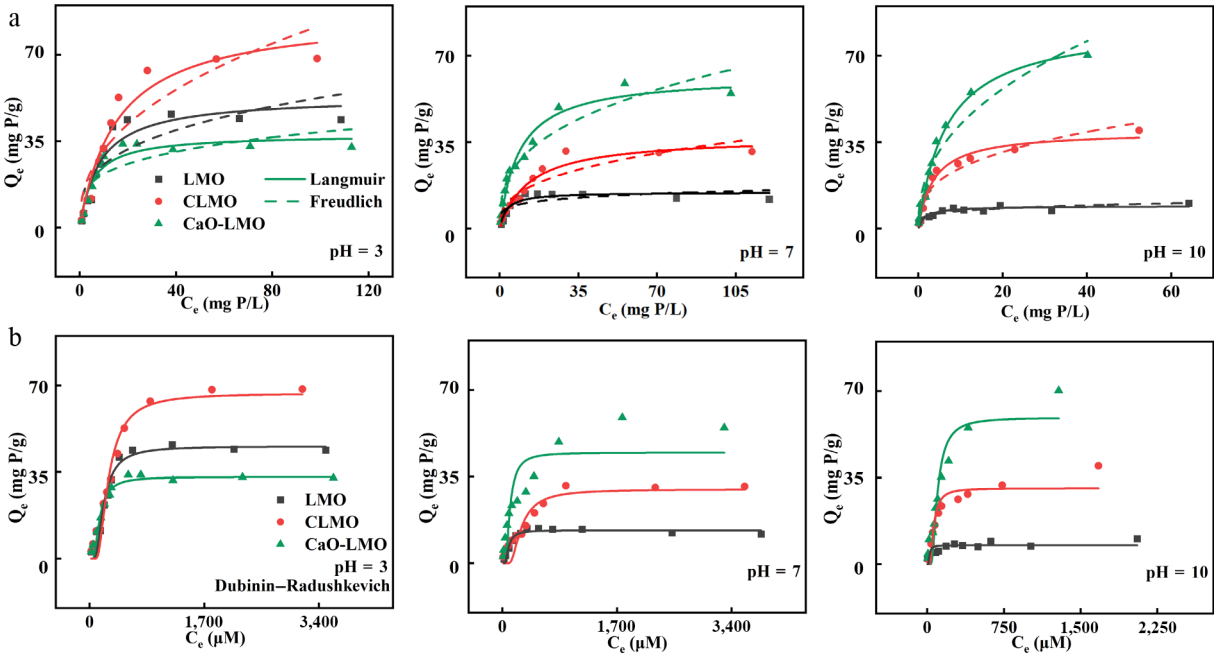

Fig. 3 (a) Langmuir, Freundlich, and (b) Dubinin–Radushkevich adsorption isotherm models of the adsorbents at pH = 3, 7, 1 and 0 (dosage: 20 mg, V = 50 mL, T = 298 K).

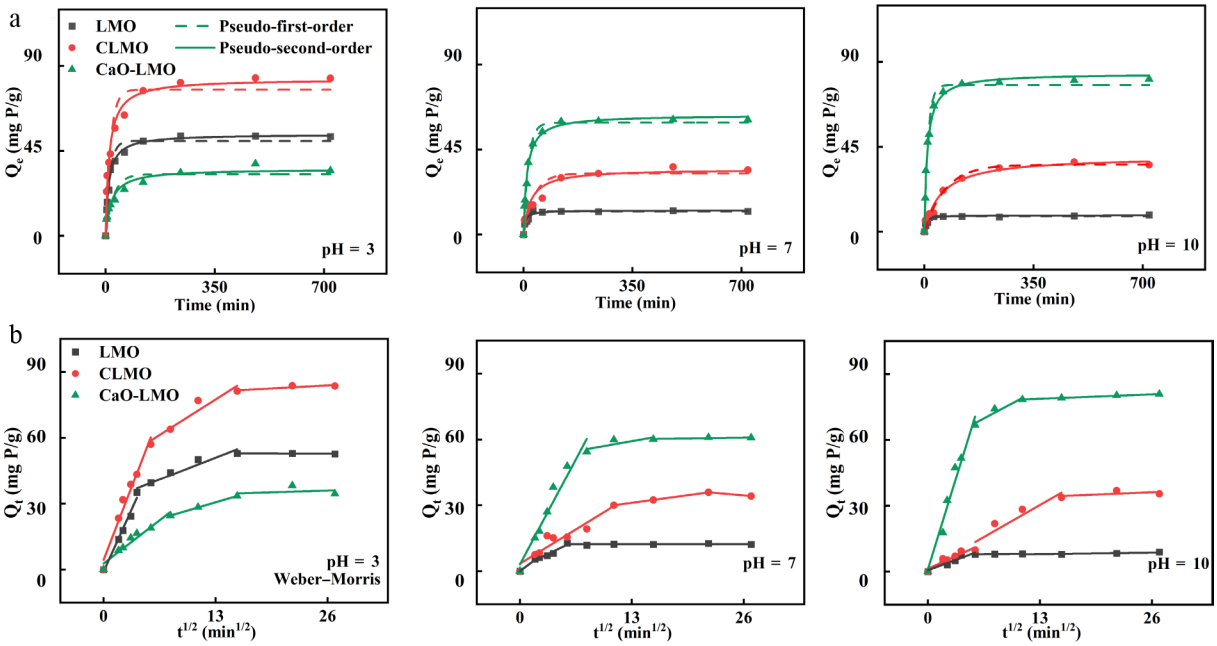

Fig. 4 (a) Pseudo-first-order, pseudo-second-order, and (b) Weber–Morris adsorption kinetic models of the adsorbents at pH = 3, 7, and 10 (dosage: 20 mg, V = 50 mL, C_0 = 150 mg/L, T = 298 K).

initial pH significantly affected the performance in terms of the adsorption of phytic acid. As the pH increases from 2 to 12, LMO and CLMO exhibit a decrease in adsorption capacity by 94.5% and 69.3%, respectively. Conversely, the adsorption capacity of CaO-LMO increased by 132.4% under the same conditions. The maximum adsorption capacities for LMO and CLMO were achieved at an initial pH of 3, and CaO-LMO reached its peak at an initial pH of 10. This discrepancy may be attributed to the higher zeta potential of LMO and CLMO compared with that of CaO-LMO in acidic conditions, which enhances electrostatic attraction. Meanwhile, CaO-LMO exhibited a high zeta potential near pH 10, resulting in relatively weak electrostatic repulsion (Fig. 1g). Postadsorption zeta potential measurements for all three adsorbents showed a downward shift compared with their preadsorption values and remained negative across the tested pH range, indicating the successful adsorption of negatively charged phytic acid.

Adsorption selectivity is an important factor influencing the practical application of phosphate adsorbents. Certain anions can compete with phosphate for active sites; however, the effect of coexisting ions on phytic acid adsorption remains unclear. This study investigated the effects of varying concentration gradients of Cl^-, CO_3^{2-}, NO_3^-, SO_4^{2-}, and NH_4^+ coexisting with phytic acid on the adsorption of the latter (Fig. 5a). The adsorption of phytic acid was unaffected by increasing concentrations of NO_3^-, Cl^-, and SO_4^{2-}, indicating that the Ca–O(H) and La–O(H) groups in the three adsorbents exhibited excellent selectivity and affinity for phytic acid adsorption. CO_3^{2-} significantly influenced phytic acid adsorption because it bound to the Ca sites on the surface of the adsorbent compared with phytic acid. Increasing NH_4^+ concentrations enhanced phytic acid adsorption because the positive charge of NH_4^+ facilitated its interaction with the negatively charged phytic acid, allowing the metals La, Ca and NH_4^+ to adsorb phytic acid and form a complex. An increase in the dose of the three adsorbents enhanced the total phosphorus removal rates in dairy farm wastewater, pond surface runoff, and domestic sewage. Compared with the maximum removal rates of LMO (50.4%–89.4%) and CLMO (76.2%–93.6%), the total phosphorus removal rates of CaO-LMO (88.77%–97.63%) were superior across all three water bodies at pH 8. Compared with the maximum removal rates of LMO (58.78%–93.33%) and CaO-LMO (79.9%–100%), the total phosphorus removal rates of CLMO (95.60%–100%) were superior across all three water bodies at pH 6. (Fig. 5b). CaO-LMO exhibits high selectivity for phosphorus in actual water bodies and can be widely applied in various neutral and alkaline phosphorus-containing wastewaters. At pH < 3, the breakthrough curves of LMO and CLMO in laboratory-scale columns (Fig. 5d) implied that the curve of CLMO shifts rightward compared with that of LMO. LMO and CLMO reached saturation at 80 and 140 min, respectively, indicating that CLMO has a significantly prolonged saturation time and increased phytic acid adsorption capacity, demonstrating its good phosphorus adsorption performance in acidic waters. The results of verification of the removal of various organic phosphates by the three adsorbents are shown in Fig. 5e, with all three effectively removing multiple organic phosphates. At the same initial organic phosphate concentration, compared with that of $LaMnO_3$, the adsorption performance of CLMO and CaO-LMO improved by 98.2% and 240%, 523% and 269%, and by 239% and 252% for G_6P, ATP, and HEDP, respectively. These results demonstrate that Ca modification enhances $LaMnO_3$'s capacity for organic phosphate adsorption.

Mechanism of Ca-doped/loaded $LaMnO_3$ for phytic acid adsorption

The SEM and energy dispersive spectrometer (EDS) results for the three adsorbents after adsorbing phytic acid are shown in Fig. 6a–d. Their surface roughness increased after adsorbing phytic acid, with the pores and surfaces being filled by the aggregates of nanoscale spherical particles to form a coalesced network, similar to that observed for the phytic acid modification of $CoFe_2O_4$[37]. Coupled with the increase in P in the EDS analysis, the formation of spherical particles indicated the successful adsorption of phytic acid onto the adsorbents' surface. After adsorption, CLMO and CaO-LMO exhibit a looser morphology than that before adsorption, possibly caused by the high concentration of phytic acid, which delays the aggregation

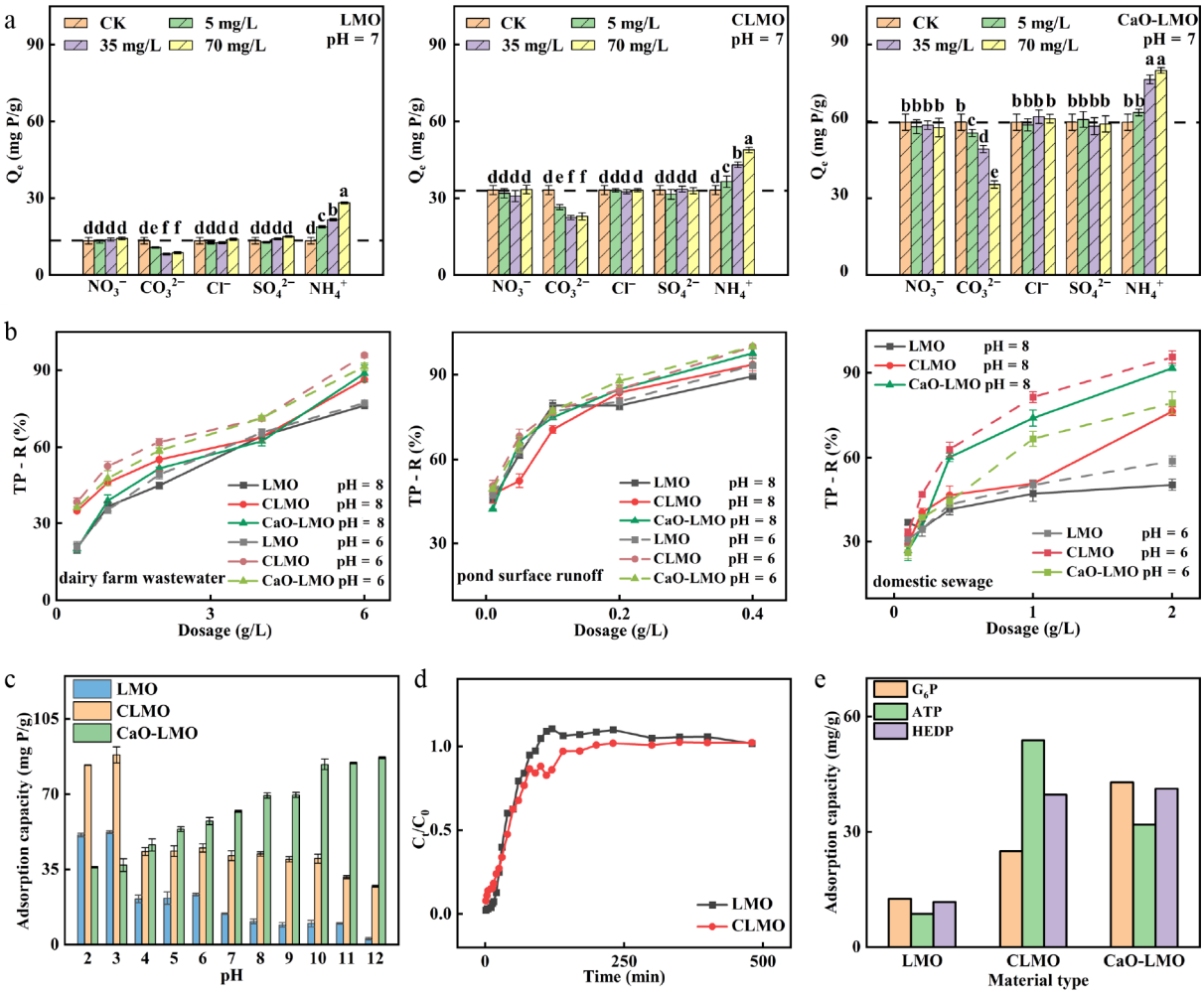

Fig. 5 (a) Adsorption performance of phytic acid by LMO, CLMO, and CaO-LMO under different coexisting ion concentrations (5, 35, and 70 mg/L) and various types of coexisting ions (NO_3^-, CO_32^-, Cl^-, SO_4^{2-}, and NH_4^+), arranged from left to right (dosage: 20 mg, volume [V] = 50 mL, C_0 = 150 mg/L, time [t] = 24 h, temperature [T] = 298 K). (b) Properties of the adsorbents used to remove total phosphorus from actual wastewater (dairy farm wastewater, pond surface runoff, and domestic sewage). (c) Effect of pH on the adsorption of phytic acid. (d) Adsorption of phytic acid on a fixed-bed column (mass [m] = 0.5 g, V = 1 L, C_0 = 100 mg/L, pH = 3, flow rate = 2 mL/min). (e) Adsorption properties of materials in different kinds of organophosphorus (m = 20 mg, pH = 7, and C_0 = 100 mg/L).

of the particles. This phenomenon is similar to the effect observed with phosphates[11]. The broadening of the XRD patterns of the three adsorbents indicated the successful adsorption of phytic acid onto their surfaces. The broadening of the $LaMnO_3$ pattern was the most pronounced, suggesting that phytic acid adsorption distorted the local environment on the $LaMnO_3$'s surface, disrupted its internal structure, and reduced its crystallinity. The XRD patterns of CLMO and CaO-LMO after phytic acid adsorption indicated that their crystallinity has not significantly decreased compared with that before adsorption, indicating that doping and loading enhance the stability of the $LaMnO_3$ structure (Fig. 6e). Changes in the zeta potential of the three adsorbents before and after adsorbing phytic acid (Fig. 1g) were attributed to the complexation of phytic acid on their surface. After adsorption, the isoelectric points of LMO, CLMO, and CaO-LMO decreased significantly compared with those before adsorption, indicating the successful adsorption of phytic acid onto their surface. A high concentration of phytic acid delivered additional negative charges to the materials' surface, forming an inner-sphere complex[38].

The FTIR spectra of the three adsorbents before and after adsorbing phytic acid are shown in Fig. 6f. The appearance of the characteristic functional groups of phytic acid, such as P = O (1,029–1,158 cm^{-1}), P–OH (909–1,030 cm^{-1}), and O–P–O (480–550 cm^{-1}), confirms the successful adsorption of phytic acid onto the surfaces of the adsorbents[39]. After adsorption, the peak intensity of the O–H band increases and its peak width broadens from 3,210–3,570 to 2,990–3,640 cm^{-1}, indicating the introduction of hydroxyl groups, potentially because of functionalization during phytic acid adsorption[40]. After adsorption, the intensity of the characteristic peaks of CO_3^{2-} (850–900 and 1,350–1,550 cm^{-1}) decreases in CaO-LMO, suggesting that the CO_3^{2-} groups of CaO-LMO undergo ion exchange with the phosphorus groups of phytic acid. The peak width of the La-O characteristic peak broadens from 827–885 to 785–885 cm^{-1}[41], and the Mn–O–Mn characteristic peak remains unchanged, indicating the involvement of La in phytic acid adsorption. Figure 7a shows the full XPS spectra of the three adsorbents after adsorbing phytic acid. La, Mn, Ca, and O were detected, and a distinct P peak appeared at approximately 133.3 eV, confirming the successful adsorption of phytic acid. Additionally, the C 1s peaks in Supplementary Fig. S5 and Supplementary Table S4 show that after the adsorption of phytic acid, LMO, CLMO, and CaO-LMO exhibit new characteristic peaks at 286.1, 286.2, and 285.9 eV, respectively,

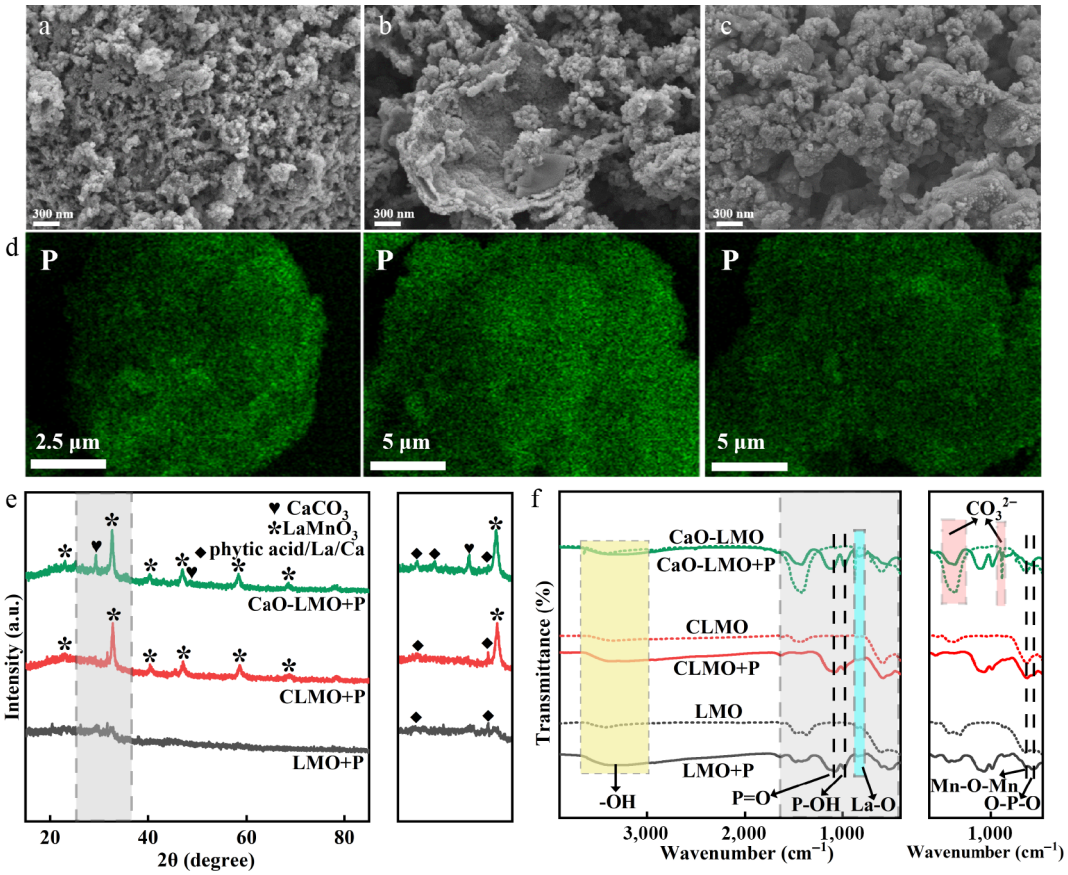

Fig. 6 SEM of samples after adsorbing phytic acid: (a) LMO, (b) CLMO, and (c) CaO-LMO. (d) Distribution of P element (pH = 3). (e) XRD spectra (please refer to Supplementary Figs. S1, S2 for enlarged images) and (f) FTIR images (the dashed and solid lines represent values before and after the adsorption of phytic acid, respectively; please refer to Supplementary Figures S3, S4 for enlarged images).

which correspond to the C-O peaks of phytic acid. After the adsorption of phytic acid, a Mn 2p peak appears, as shown in Supplementary Fig. S6, and there is no significant change compared with that before adsorption. The presence of both the P peaks and the C–O peaks confirm the successful adsorption of phytic acid. Figure 7a–e displays the fine XPS spectra of La 3d, Ca 2p, O 1s, and P 2p. The spectra of La 3d and Ca 2p (Fig. 7b, c) revealed that after phytic acid adsorption, the main peaks of La 3d3/2 and La 3d5/2 were at 833.9–835.6 and 837.8–838.9 eV, respectively, and the peaks of Ca 2p1/2 and Ca 2p3/2 were at 349.6–350.9 eV and 346.3–347.3 eV, respectively. No change in the chemical states of La and Ca was observed before and after adsorption. After phytic acid adsorption, ΔLa 3d decreased from 3.9, 4.1, and 3.7 eV to 3.3, 3.3, and 3.5 eV for LMO, CLMO, and CaO-LMO, respectively. Along with the appearance of a characteristic P peak in the spectra, the decrease in ΔLa 3d, which is highly sensitive to the chemical state of La, suggests the formation of a new lanthanum–phosphorus compound. The reduction in the peak areas of La and Ca indicates that phytic acid occupies the metal binding sites, forming La–O–P and Ca–O–P complexes. After phytic acid adsorption, the La 3d and Ca 2p peaks in all three adsorbents (LMO, CLMO, and CaO-LMO) shift toward higher binding energies, indicating that the valence band electrons of La 3d and Ca 2p have flown out of the system[11], reducing the electron cloud density on La and Ca and transferring electrons to the phytic acid. The binding energy shifts of the La 3d peaks in LMO, CLMO, and CaO-LMO were 1.4, 1.7, and 0.9 eV, respectively, and those of the Ca 2p peaks were 1.0 and 0.1 eV. The order of electron transfer capability from La/Ca to phytic acid was CLMO > LMO > CaO-LMO, which is consistent with the adsorption capacity results[42]; this finding indicates that La and Ca are crucial active sites affecting the adsorption of phytic acid by CLMO[20]. The O 1s spectra (Fig. 7d) revealed that the O 1s bands in the three adsorbents could be deconvoluted into two characteristic peaks: Lattice oxygen (O_{latt}) at 529.2–529.3 eV and adsorbed oxygen (O_{ads}) in the surface oxygen vacancies at 531.2–531.3 eV. After phytic acid adsorption, these bands deconvoluted into three peaks: O_{latt} (531.1–531.3 eV), O_{ads} (532.6–532.9 eV), and H_2O (536.1–536.3 eV). The shift of the O 1s peaks toward high binding energies in all three adsorbents indicated a decrease in the electron density of O atoms[35], suggesting that O participates in the adsorption reaction and electron transfer. The surface lattice oxygen concentration (adsorbed oxygen concentration) was calculated as the area ratio of $O_{latt}(O_{ads})/O_{all}$[43]. The results showed that after phytic acid adsorption, the proportion of O_{latt} in LMO, CLMO, and CaO-LMO increases from 43%, 50%, and 21% to 58%, 62%, and 60%, respectively, indicating the formation of Ca–O–P, La–O–P, and inner-sphere complexation between phytic acid and the adsorbents, which is consistent with the findings of Feng et al. on phosphate adsorption[20]. The proportion of O_{ads} significantly decreased from 57%, 50%, and 79% to 36%, 50%, and 30%, indicating that adsorption of phytic acid consumed a large number of oxygen vacancies[44], and phytic acid preferentially bonded with the electrons provided by the adsorbed oxygen. In summary, these findings indicate that oxygen participates in the adsorption reaction, leading to electron transfer, with the phosphorus in phytic

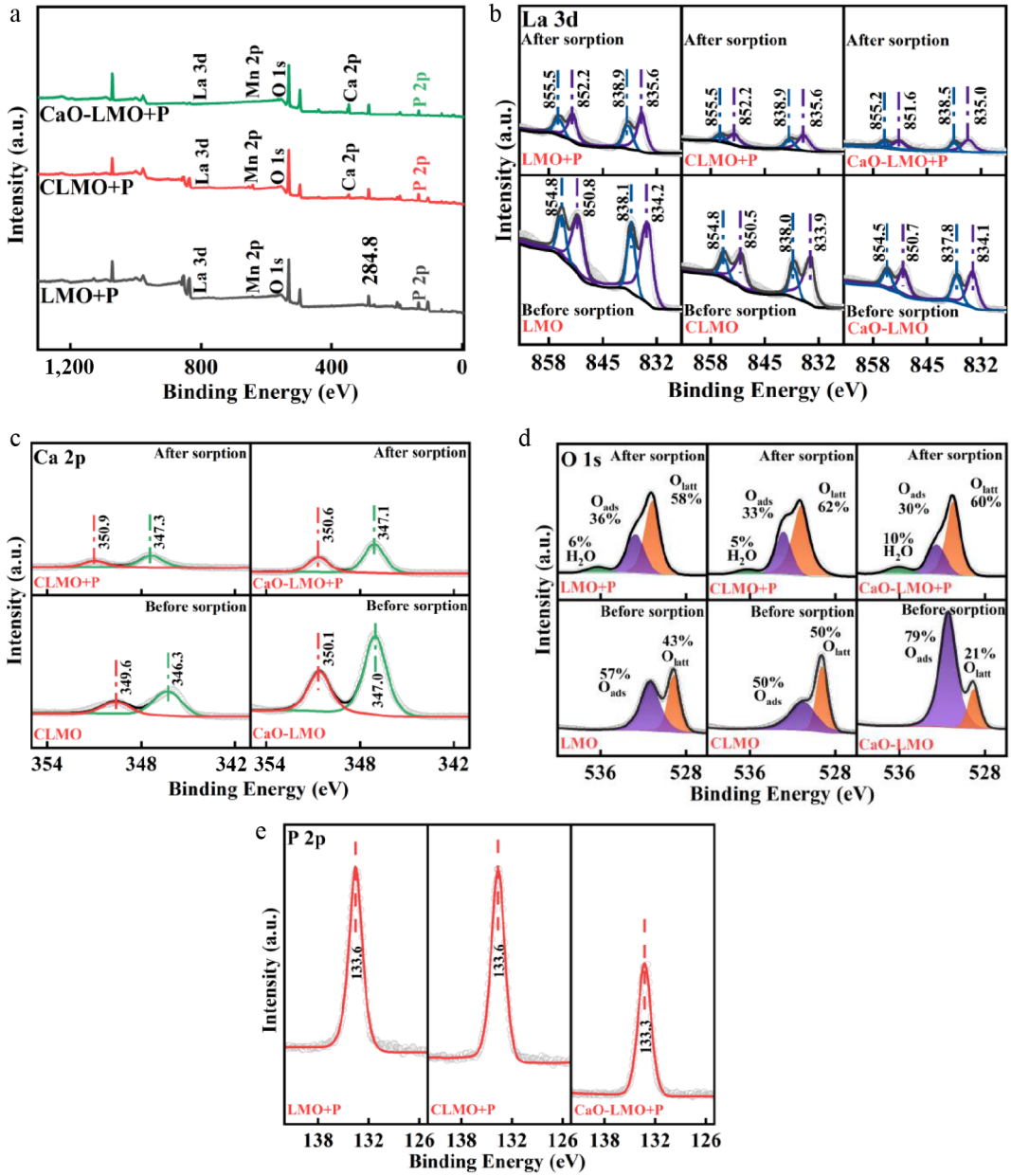

Fig. 7 XPS spectra before and after adsorption of phytic acid by the adsorbents: (a) Full spectra, (b) La 3d, (c) Ca 2p (only CLMO and CaO-LMO are presented), (d) O 1s, and (e) P 2p. All peaks were corrected by the C 1s peak (284.8 eV) and subjected to deconvolution.

acid preferentially bonding with the electrons provided by the adsorbed oxygen. Lattice oxygen is activated into adsorbed oxygen through the induction of oxygen vacancies, which is subsequently consumed by the adsorption of phytic acid. The P 2p binding energy of LMO and CLMO is higher than that of CaO-LMO P 2p, indicating that LMO and CLMO adsorb more P and O in phytic acid to form a coordination[35]. The XPS results are consistent with those from FTIR and further confirm the coordination between phytic acid and the adsorbents.

Conclusions

The structural change in $LaMnO_3$ upon Ca doping and loading results in an expansion of phytic acid adsorption sites from solely La positions to multiple active centers, including La, Ca, and O. Consequently, the adsorption performance is considerably enhanced. Batch adsorption tests revealed that the Langmuir and Dubinin–Radushkevich models can adequately describe the adsorption of phytic acid by LMO, CLMO, and CaO-LMO. The pH emerges as the predominant factor affecting phytic acid adsorption: CLMO exhibits the highest adsorption capacity in acidic aqueous environments, reaching 86.54 mg P/g at pH = 3, whereas CaO-LMO demonstrates the highest adsorption performance in neutral to alkaline conditions, reaching 83.20 mg P/g at pH = 10. Practical wastewater treatment and fixed-bed column tests also substantiated that CLMO is suitable for acidic environments and CaO-LMO is preferable for neutral to alkaline conditions. All three adsorbents show broad applicability in adsorbing various organophosphorus compounds. The primary mechanisms of phytic acid adsorption by the three perovskites include ligand exchange, inner-sphere complexation, and electrostatic attraction. In Ca-loaded $LaMnO_3$, the La/Ca sites serve as active adsorption sites for phytic acid. In Ca-doped $LaMnO_3$, the La/Ca sites and oxygen vacancies are the adsorption sites. By contrast, $LaMnO_3$

only has the La sites as the adsorption sites. Ca doping and loading enhance the structural stability of $LaMnO_3$ for adsorbing phytic acid. This study recommends the use of Ca-doped $LaMnO_3$ for removing organic phosphorus in acidic waters and Ca-loaded $LaMnO_3$ for alkaline waters.

Author contributions

The authors confirm their contributions to the paper as follows: writing – original draft, conceptualization: Feng M; methodology: Feng M, Luo Y; software: Feng M, Yuan T, Fu W; writing – review and editing: Lv S, Fu W; data curation: Feng M, Lv S; resources: Lv S; visualization: Zhang X; investigation: Zhang X, Luo Y; supervision: Guo C; validation: Yuan T; formal analysis: Guo C, Zhou J; funding acquisition, project administration: Wang F. All authors reviewed the results and approved the final version of the manuscript.

Data availability

The datasets generated during and/or analyzed in the current study are available from the corresponding author on reasonable request.

Acknowledgments

This work was supported by the Agricultural Science and Technology Innovation Program (Agro-Environmental Protection Institute, Ministry of Agriculture and Rural Affairs), the Macao Centre for Research and Development in Advanced Materials (University of Macau) (Ref. No.: CAM-IAPME(UM)/ORP/2026/00X), Hulunbuir City Science and Technology Plan Project (SF2025004), the National Key Research and Development Program of China (2022YFD1901305), Yunnan Fundamental Research Projects (202101AT070002), Wangfeng Expert Primary-level Workstation, Yunnan Province, Intelligent aid to Xinjiang Innovation and Development Talent Plan ("Group Group" aid team), and Environmental Functional Materials Development and Agricultural Applications.

Conflict of interest

The authors declare that they have no conflict of interest.

Supplementary information accompanies this paper online at: https://doi.org/10.48130/prkm-0026-0007.

Dates

Received 25 November 2025; Revised 4 January 2026; Accepted 12 February 2026; Published online 28 May 2026

References

[1] Sharma N, Angural S, Rana M, Puri N, Kondepudi KK, et al. 2020. Phytase producing lactic acid bacteria: cell factories for enhancing micronutrient bioavailability of phytate rich foods. *Trends in Food Science & Technology* 96:1–12

[2] Park EY, Lim ST. 2019. Characterization of waxy starches phosphorylated using phytic acid. *Carbohydrate Polymers* 225:115225

[3] Acuña-Alonso C, Álvarez X, Lorenzo O, Cancela Á, Valero E, et al. 2020. Assessment of water quality in eutrophized water bodies through the application of indexes and toxicity. *Science of the Total Environment* 728:138775

[4] Uzun HI, Debik E. 2019. Economical approach to nitrate removal via membrane capacitive deionization. *Separation and Purification Technology* 209:776–781

[5] Wang Y, Kuntke P, Saakes M, van der Weijden RD, Buisman CJN, et al. 2022. Electrochemically mediated precipitation of phosphate minerals for phosphorus removal and recovery: progress and perspective. *Water Research* 209:117891

[6] Liu X, Han R, Cao Y, Turner BL, Ma LQ. 2022. Enhancing phytate availability in soils and phytate-P acquisition by plants: a review. *Environmental Science & Technology* 56:9196–9219

[7] Filippovich SY, Isakova EP, Gessler NN, Deryabina YI. 2023. Advances in immobilization of phytases and their application. *Bioresource Technology* 379:129030

[8] Zhao D, Qiu SK, Li MM, Luo Y, Zhang LS, et al. 2022. Modified biochar improves the storage capacity and adsorption affinity of organic phosphorus in soil. *Environmental Research* 205:112455

[9] Yang B, Wang D, Cao S, Yin W, Xue J, et al. 2020. Selective adsorption of a high-performance depressant onto dolomite causing effective flotation separation of magnesite from dolomite. *Journal of Colloid and Interface Science* 578:290–303

[10] Le QTN, Cho K. 2021. Caesium adsorption on a zeolitic imidazolate framework (ZIF-8) functionalized by ferrocyanide. *Journal of Colloid and Interface Science* 581:741–750

[11] Chen A, Li Y, Shang J, Arai Y. 2020. Ferrihydrite transformation impacted by coprecipitation of phytic acid. *Environmental Science & Technology* 54:8837–8847

[12] Kremer C, Torres J, Bianchi A, Savastano M, Bazzicalupi C. 2020. Myo-inositol hexakisphosphate: coordinative versatility of a natural product. *Coordination Chemistry Reviews* 419:213403

[13] Xie F, Dong G, Wu M, Wu K, Huang C, et al. 2023. Iodine-doped g-C_3N_4 modified zinc titanate electron transporting layer for highly efficient perovskite solar cells. *Journal of Colloid and Interface Science* 635:159–166

[14] Niu J, Liland SE, Yang J, Rout KR, Ran J, et al. 2019. Effect of oxide additives on the hydrotalcite derived Ni catalysts for CO_2 reforming of methane. *Chemical Engineering Journal* 377:119763

[15] Feng M, Li M, Guo C, Yuan M, Zhang L, et al. 2024. Green synthesis of $Ca_xLa_{1-x}MnO_3$ with modulation of mesoporous and vacancies for efficient low concentration phosphate adsorption. *Journal of Environmental Management* 351:119837

[16] Zhang P, He M, Li F, Fang D, Li C, et al. 2024. Unlocking bimetallic active centers via heterostructure engineering for exceptional phosphate electrosorption: internal electric field-induced electronic structure reconstruction. *Environmental Science & Technology* 58:2112–2122

[17] Li M, Feng M, Guo C, Qiu S, Zhang L, et al. 2023. Green and efficient Al-doped $LaFe_xAl_{1-x}O_3$ perovskite oxide for enhanced phosphate adsorption with creation of oxygen vacancies. *ACS Applied Materials & Interfaces* 15:16942–16952

[18] Behara S, Thomas T. 2020. Stability and amphotericity analysis in rhombohedral ABO_3 perovskites. *Materialia* 13:100819

[19] Su H, Liu Y, Ren Q, Shen Z, Guo M, et al. 2023. Unveiling the dynamic instability mechanism of microstructure transformation in faceted oxide eutectic composite ceramics. *Journal of Materials Science & Technology* 144:224–234

[20] Liao T, Li T, Su X, Yu X, Song H, et al. 2018. $La(OH)_3$-modified magnetic pineapple biochar as novel adsorbents for efficient phosphate removal. *Bioresource Technology* 263:207–213

[21] Feng M, Li M, Guo C, Zhang X, Yuan T, et al. 2024. Composites hybridized with $Ca(OH)_2$ and $LaMnO_3$ synergistically improve phosphate adsorption properties. *New Journal of Chemistry* 48:2155–2165

[22] Hamid A, Wilson AE, Torbert HA, Wang D. 2023. Sorptive removal of phosphorus by flue gas desulfurization gypsum in batch and column systems. *Chemosphere* 320:138062

[23] Santos AF, Lopes DV, Alvarenga P, Gando-Ferreira LM, Quina MJ. 2024. Phosphorus removal from urban wastewater through adsorption using biogenic calcium carbonate. *Journal of Environmental Management* 351:119875

[24] Thenmozhi N, Saravanan R. 2022. High-temperature synthesis and electronic bonding analysis of Ca-doped $LaMnO_3$ rare-earth manganites. *Rare Metals* 41:3932–3942

[25] Yoo Y, Kang D, Park S, Park J. 2020. Carbon utilization based on post-treatment of desalinated reject brine and effect of structural properties of amines for $CaCO_3$ polymorphs control. *Desalination* 479:114325

[26] Londoño-Calderón V, Rave-Osorio LC, Restrepo J, Játiva J, Jurado JF, et al. 2018. Structural and magnetic properties of $La_{1-x}(Ca, Sr)_xMnO_3$ powders produced by the hydrothermal method. *Journal of Superconductivity and Novel Magnetism* 31:4153–4162

[27] Yusuf M, Ali Khan M, Abdullah EC, Elfghi M, Hosomi M, et al. 2016. Dodecyl sulfate chain anchored mesoporous graphene: synthesis and application to sequester heavy metal ions from aqueous phase. *Chemical Engineering Journal* 304:431–439

[28] Weng Z, Liu L, Hu Y, Wei Y, Da P, et al. 2024. Significance of engineering the MnO_6 octahedral units to promote the oxygen reduction reaction of perovskite oxides. *Advanced Materials* 36:2311102

[29] Zhang C, Wang Y, Lin X, Wu T, Han Q, et al. 2021. Effects of A site doping on the crystallization of perovskite films. *Journal of Materials Chemistry A* 9:1372–1394

[30] Shi Z, Li H, Zhang L, Cao Y. 2022. Improved photocatalytic activity of $LaFeO_3$ with doping Mn^{3+} ions and modifying Pd^{2+} ions for photoreduction of CO_2 into CH_4. *Journal of Power Sources* 519:230738

[31] Zhang T, Zhao Y, Bai H, Wang W, Zhang Q. 2019. Enhanced arsenic removal from water and easy handling of the precipitate sludge by using $FeSO_4$ with $CaCO_3$ to $Ca(OH)_2$. *Chemosphere* 231:134–139

[32] Tan J, Ren H, Zhao Z, Xin X, Shi Y, et al. 2023. Ca^{2+} doped metal organic frameworks for enhanced photocatalytic ammonia synthesis. *Chemical Engineering Journal* 466:143259

[33] Bai H, Wang Z, Zhang J, Wu J, Yue Y, et al. 2021. Synthesis of a perovskite-type catalyst from Cr electroplating sludge for effective catalytic oxidization of VOC. *Journal of Environmental Management* 294:113025

[34] Wang Q, Luo C, Li X, Ding H, Shen C, et al. 2019. Development of $LaFeO_3$ modified with potassium as catalyst for coal char CO_2 gasification. *Journal of CO_2 Utilization* 32:163–169

[35] Chen D, He D, Lu J, Zhong L, Liu F, et al. 2017. Investigation of the role of surface lattice oxygen and bulk lattice oxygen migration of cerium-based oxygen carriers: XPS and designed H_2-TPR characterization. *Applied Catalysis B: Environmental* 218:249–259

[36] Wang Z, Huang X, Jia Y, Guo L, Wang H, et al. 2024. Localized surface plasmon resonance-induced bidirectional electron transfer of formic acid adsorption for boosting photocatalytic hydrogen production on Ni/TiO_2. *Chemical Engineering Journal* 482:148942

[37] Hu Q, Ma S, He Z, Liu H, Pei X. 2024. A revisit on intraparticle diffusion models with analytical solutions: Underlying assumption, application scope and solving method. *Journal of Water Process Engineering* 60:105241

[38] Cai K, Shen W, Ren B, He J, Wu S, et al. 2017. A phytic acid modified $CoFe_2O_4$ magnetic adsorbent with controllable morphology, excellent selective adsorption for dyes and ultra-strong adsorption ability for metal ions. *Chemical Engineering Journal* 330:936–946

[39] Li L, Stanforth R. 2000. Distinguishing adsorption and surface precipitation of phosphate on goethite (α-FeOOH). *Journal of Colloid and Interface Science* 230:12–21

[40] Lu X, Zhang Y, Cheng W, Liu Y, Wu X, et al. 2022. Experimental and computational study on the inhibitory effect of phytic acid on U(VI) biomineralization by *Shewanella putrefaciens*. *Chemical Engineering Journal* 450:138364

[41] Karthikeyan S, Parthibavarman M, Mohammed MKA, Mohammed SH, Selvapandiyan M, et al. 2022. Morphology and vibrational modes of lanthanum oxide (La_2O_3) nanoparticles prepared with reflux routes at different reaction times. *Chemistry Africa* 5:1427–1432

[42] Li Z, Xiong J, Song H, Liu S, Huang Y, et al. 2024. Synergistically enhancing CO_2 adsorption/activation and electron transfer in ZIF-67/$Ti_3C_2T_x$ MXene for boosting photocatalytic CO_2 reduction. *Separation and Purification Technology* 341:126817

[43] Chon B, Lee HJ, Kang Y, Kim HW, Kim CH, et al. 2024. Investigation of interface characteristics and physisorption mechanism in quantum dots/TiO_2 composite for efficient and sustainable photoinduced interfacial electron transfer. *ACS Applied Materials & Interfaces* 16:9414–9427

[44] Wang Q, Ma L, Wang L, Wang D. 2019. Mechanisms for enhanced catalytic performance for NO oxidation over La_2CoMnO_6 double perovskite by A-site or B-site doping: effects of the B-site ionic magnetic moments. *Chemical Engineering Journal* 372:728–741